



OPEN

## g-C<sub>3</sub>N<sub>4</sub>/Ca<sub>2</sub>Fe<sub>2</sub>O<sub>5</sub> heterostructures for enhanced photocatalytic degradation of organic effluents under sunlight

Durga Sankar Vavilapalli<sup>1</sup>, Raja Gopal Peri<sup>2</sup>, R. K. Sharma<sup>3</sup>, U. K. Goutam<sup>3</sup>, B. Muthuraaman<sup>2</sup>, M. S. Ramachandra Rao<sup>4</sup> & Shubra Singh<sup>1</sup>✉

g-C<sub>3</sub>N<sub>4</sub>/Ca<sub>2</sub>Fe<sub>2</sub>O<sub>5</sub> heterostructures were successfully prepared by incorporating g-C<sub>3</sub>N<sub>4</sub> into Ca<sub>2</sub>Fe<sub>2</sub>O<sub>5</sub> (CFO). As prepared g-C<sub>3</sub>N<sub>4</sub>/CFO heterostructures were initially utilized to photodegrade organic effluent Methylene blue (MB) for optimization of photodegradation performance. 50% g-C<sub>3</sub>N<sub>4</sub> content in CFO composition showed an enhanced photodegradation efficiency (~96%) over g-C<sub>3</sub>N<sub>4</sub> (48.15%) and CFO (81.9%) due to mitigation of recombination of photogenerated charge carriers by Type-II heterojunction. The optimized composition of heterostructure was further tested for degradation of Bisphenol-A (BPA) under direct sunlight, exhibiting enhanced photodegradation efficiency of about 63.1% over g-C<sub>3</sub>N<sub>4</sub> (17%) and CFO (45.1%). The photoelectrochemical studies at various potentials with and without light illumination showed significant improvement in photocurrent response for g-C<sub>3</sub>N<sub>4</sub>/Ca<sub>2</sub>Fe<sub>2</sub>O<sub>5</sub> heterostructures (~1.9 mA) over CFO (~67.4 μA). These studies revealed efficient solar energy harvesting ability of g-C<sub>3</sub>N<sub>4</sub>/Ca<sub>2</sub>Fe<sub>2</sub>O<sub>5</sub> heterostructures to be utilized for organic effluent treatment.

Energy and environmental crisis arising due to rapid industrialization, leads to organic/inorganic pollutants originating from textile, printing, polymer and pharmaceutical industries<sup>1</sup>. Purification of such pollutants should be carried out prior to being released into water bodies. Dyes like Methylene blue (MB), Congo red (CR) etc. and synthetic compounds like Bisphenol-A [2,2-bis (4-hydroxyphenyl) propane] or BPA are some of the widely used chemicals in industries<sup>2–4</sup>. Organic pollutants such as BPA etc. have been extensively detected in wastewater bodies, severely impact on human health<sup>2–4</sup>. BPA is one of the important raw materials for epoxy and polycarbonate plastics (e.g., coatings of water containers, infant bottles, and medical devices)<sup>5</sup>. It is extensively found in water, air and soil and acts as an endocrine-disrupting chemical. Exposure of BPA can induce carcinogenic and epigenetic modifications in humans<sup>6</sup>. In actual environmental conditions it's difficult to degrade these pollutants into small non-toxic molecules<sup>7</sup>. Various technologies such as filtration, phytoremediation and adsorption etc., which have been adopted to treat these pollutants from wastewater, are less efficient, high cost as well consume huge energy<sup>8–10</sup>. Hence, it is imperative to develop clean, green and efficient methods to treat these organic pollutants by environmental friendly methods. Sunlight driven photocatalysis is one such efficient, cost-effective and environmental friendly physicochemical method to remove these pollutants from waste waters. Efficient photocatalysts are required for solar energy harvesting to treat pollutant through photocatalysis. Semiconductor based photocatalysts such as TiO<sub>2</sub> and ZnO are widely used photocatalysts for water purification<sup>11–15</sup>. Since these materials have low photoactivity due to wider bandgap (absorbing only UV-light from solar spectrum)<sup>16</sup>, it is necessary to develop efficient visible light active photocatalysts for water purification. We come across some visible light active perovskite structured metal-oxide based photocatalysts such as MTiO<sub>3</sub> (M: Fe, Co, Ni, Pb, Mn), LaFeO<sub>3</sub>, BiFeO<sub>3</sub>, LaCoO<sub>3</sub>, YFeO<sub>3</sub>, AgNbO<sub>3</sub>, NaTaO<sub>3</sub>, LaNiO<sub>3</sub>, etc., which showed significant photocatalytic performance for degrading organic effluents<sup>17–28</sup>. However, the performance of such perovskite catalysts is limited by recombination of photogenerated charge carriers. The charge recombination phenomenon can be suppressed by doping with metallic or non-metallic dopants and formation of heterojunction catalysts<sup>29</sup>. Heterojunctions based on semiconductor composites have been reported to be effective as efficient photocatalysts by

<sup>1</sup>Crystal Growth Centre, Anna University, Chennai 600025, India. <sup>2</sup>Department of Energy, University of Madras, Chennai 600025, India. <sup>3</sup>Technical Physics Division, Bhabha Atomic Research Centre, Mumbai 400085, India. <sup>4</sup>Nano Functional Materials Technology Centre and Department of Physics, Indian Institute of Technology Madras, Chennai 600036, India. ✉email: shubra6@gmail.com

suppressing electron–hole pair recombination<sup>30</sup>. In this regard, Graphitic carbon nitride (g-C<sub>3</sub>N<sub>4</sub>) is an important candidate for a metal-free heterogeneous catalyst due to its robust stability and visible light responsiveness. The catalytic performance of g-C<sub>3</sub>N<sub>4</sub> alone is unsatisfactory due to limited active sites and poor electron–hole pair separation<sup>31–33</sup>. Hence, a heterojunction based on metal-oxides and g-C<sub>3</sub>N<sub>4</sub> could be an effective strategy to enhance photocatalytic performance. Brownmillerite Ca<sub>2</sub>Fe<sub>2</sub>O<sub>5</sub> (CFO) is a multifunctional metal oxide which has wide range of applications in CO<sub>2</sub> capturing, energy storage, fuel cells and photocatalysis etc.<sup>34–36</sup>. Relatively lower bandgap along with ordered oxygen vacancies in these brownmillerites is expected to be advantageous for photocatalytic applications. Oxygen vacancies in these brownmillerites can act as photoinduced charge traps to suppress the recombination of photogenerated charge carriers<sup>34,37</sup>. Further, the photodegradation efficiency of these compounds can be enhanced by forming heterojunction with g-C<sub>3</sub>N<sub>4</sub>. These g-C<sub>3</sub>N<sub>4</sub>/CFO heterojunctions are expected to enhance the photodegradation efficiency by efficient solar energy harvesting, improving stability and charge separation.

Therefore, in this work simple and facile synthesis of g-C<sub>3</sub>N<sub>4</sub>/CFO heterojunctions is revealed, and its morphological, structural and optical properties are investigated. The photocatalytic performance of g-C<sub>3</sub>N<sub>4</sub>/CFO heterojunctions were analyzed by degrading organic effluents MB and BPA under natural sunlight. In order to examine the photoactivity of g-C<sub>3</sub>N<sub>4</sub>/CFO composites, photoelectrochemical (PEC) studies were carried out and compared with the PEC performance of bare CFO. Systematic studies were carried out to test the performance of g-C<sub>3</sub>N<sub>4</sub>/CFO composites for solar energy harvesting applications.

## Experimental

**Material preparation.** Brownmillerite nano Ca<sub>2</sub>Fe<sub>2</sub>O<sub>5</sub> (CFO) was synthesized using chemical route method, as explained in previous reports<sup>34,37</sup>. g-C<sub>3</sub>N<sub>4</sub> was synthesized by heat treatment of melamine in a box furnace. Melamine was first taken into a partially closed alumina crucible and then heated to 550 °C with a heating rate of 2 °C/min for 4 h followed by cooling down to room temperature<sup>32</sup>. The yellowish g-C<sub>3</sub>N<sub>4</sub> mass was ground into fine powder. g-C<sub>3</sub>N<sub>4</sub>/CFO heterostructures were prepared by grinding CFO and g-C<sub>3</sub>N<sub>4</sub> together with different contents of g-C<sub>3</sub>N<sub>4</sub> in CFO at 10%, 25%, 50% and 75% followed by heat treatment at 300 °C. These samples were further named as CCN10, CCN25, CCN50 and CCN75 respectively.

**Characterization.** Room temperature X-ray diffraction pattern of as prepared samples were recorded by Bruker D2 X-ray Diffractometer using Cu K $\alpha$  radiation. The microstructure and elemental mapping of as-synthesized samples were recorded using scanning electron microscope (SEM, Jeol, 20 kV) and Energy-dispersive X-ray spectroscopy (EDS) respectively. Optical absorption spectra and concentration of effluents was analyzed using UV–visible spectroscopy (Jasco V-730). The X-ray photoelectron spectra of as synthesized samples were recorded using bending magnet based Hard X-ray Photoelectron Spectroscopy Beamline at Indus-2 synchrotron source facility at RRCAT, Indore<sup>38</sup>.

**Photocatalytic degradation of MB and BPA.** The photocatalytic performance of these heterostructures was investigated during degradation of organic effluent Methylene blue (MB) and polycarbonate plasticizer Bisphenol-A (BPA) under natural sunlight. The MB dye solution was prepared with a concentration of  $1 \times 10^{-5}$  M. 50 mg of catalyst was loaded to 100 ml of dye solution. The catalyst dye solution was ultrasonicated and placed in dark for 20 min to achieve dark adsorption equilibrium. No significant degradation of MB could be observed under dark condition. The dye catalyst solution was then placed under sunlight. At every 10 min interval the dye catalyst solution was collected and centrifuged to collect the catalyst followed by simultaneous measurement of concentration of dye solution by UV–vis absorption spectroscopy. The BPA solution with a concentration of 50 mg/L was prepared by dissolving commercially available BPA (Sigma-Aldrich, >99%) in water. 50 mg of catalyst was loaded for 100 ml of BPA solution. The catalyst-BPA suspension was kept in sunlight and the sample was collected in regular intervals. Concentration of BPA was measured by UV–Vis absorption spectroscopy eventually. The percentage of photodegradation and first order rate constants of all samples are measured using expressions-1 and 2.

$$\text{Percentage of Degradation (\%D)} = \left[ \frac{C_0 - C}{C_0} \right] \quad (1)$$

$$\ln \frac{C_0}{C} = kt \quad (2)$$

where  $C_0$  and  $C$  are the concentrations of effluent at 0 min and at corresponding time interval respectively.  $k$  is the degradation rate constant.

**Photoelectrochemical (PEC) studies.** Photoelectrochemical (PEC) performance of CFO and g-C<sub>3</sub>N<sub>4</sub>/CFO composite was investigated using Electrochemical workstation (Autolab, PGSTAT 204 FRA32M) under illumination of 100 mW/cm<sup>2</sup> (1 Sun) of light intensity. Photoelectrodes are prepared by coating slurry of active material on FTO (a mixture of  $\alpha$ -terpineol and ethyl cellulose mixture used as binder).

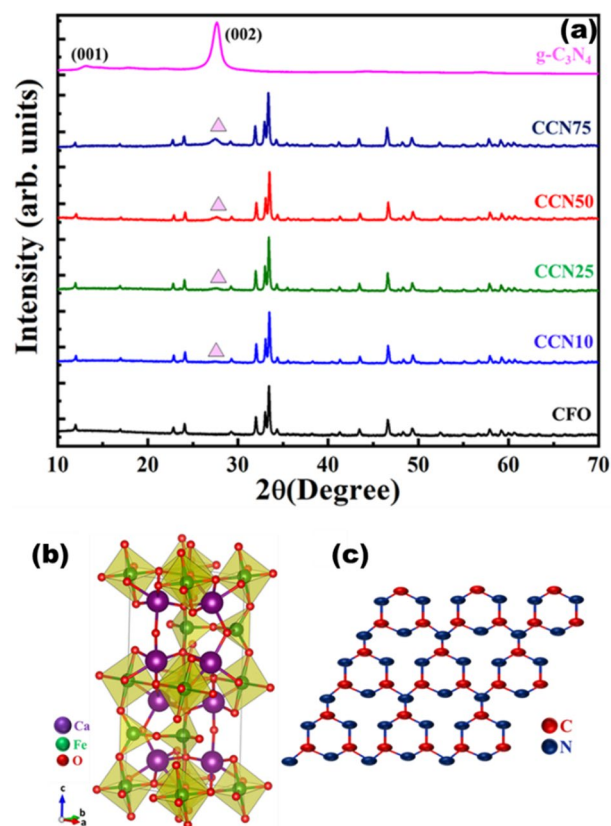


**Figure 1.** (a) XRD pattern of the CFO,  $g\text{-C}_3\text{N}_4$ , CCN10, CCN25, CCN50 and CCN75. (b and c) Structures of brownmillerite  $\text{Ca}_2\text{Fe}_2\text{O}_5$  and layered  $g\text{-C}_3\text{N}_4$  respectively.

## Results and discussion

Structural phase analysis of  $\text{Ca}_2\text{Fe}_2\text{O}_5$ ,  $g\text{-C}_3\text{N}_4$  and  $g\text{-C}_3\text{N}_4/\text{CFO}$  composites was carried out by powder XRD as shown in Fig. 1(a). The XRD pattern of CFO is in good agreement with orthorhombic crystal system (Fig. 1(b))<sup>35</sup>. XRD pattern of  $g\text{-C}_3\text{N}_4$  consists of two diffraction peaks at  $13.1^\circ$  and  $26.7^\circ$  which correspond to characteristic lattice planes (001) and (002) respectively<sup>39</sup>. The stacked 2-dimensional graphite like structure of  $g\text{-C}_3\text{N}_4$  is shown in Fig. 1(c). With increase in  $g\text{-C}_3\text{N}_4$  content in  $g\text{-C}_3\text{N}_4/\text{CFO}$  composite from 10 to 75%, the intensity of diffraction peaks corresponding to  $g\text{-C}_3\text{N}_4$  increased gradually without further secondary phase formation.

Morphology of CFO,  $g\text{-C}_3\text{N}_4$  and  $g\text{-C}_3\text{N}_4/\text{CFO}$  composite (CCN50) samples are shown in Fig. 2(a-c). EDS analysis was carried out to investigate the distribution of constituent elements in composite CCN50. From elemental mapping, uniform distribution of Ca, Fe, O, C and N elements were observed throughout the sample (Fig. 2(d-i)).

The chemical composition and the oxidation states of constituent elements were analyzed using XPS. XPS measurements of CFO and CCN50 samples were shown in Fig. 3(a-h). XPS spectra of Ca 2p of CFO and CCN50 shown in Fig. 3(a&d) constitute of two peaks arising from spin orbit coupling of Ca  $2p_{3/2}$  and Ca  $2p_{1/2}$ . In CFO, Ca  $2p_{3/2}$  and Ca  $2p_{1/2}$  peaks appeared at  $\sim 345.7$  eV and  $\sim 349$  eV respectively with a difference of  $\sim 3.3$  eV. For CCN50 samples, Ca 2p spin orbit splits into two peaks and lies at  $\sim 346.5$  eV and  $\sim 350.1$  eV with a binding energy difference of  $\sim 3.5$  eV. This implies that, in both CFO and CCN50 samples Ca existed in 2+ oxidation state<sup>35</sup>. The XPS spectra of Fe 2p for CFO and CCN50 are shown in Fig. 3(b&e). The peaks arising due to spin orbits split namely Fe  $2p_{3/2}$  and Fe  $2p_{1/2}$ , are further deconvoluted into two peaks, corresponding to octahedral ( $\text{FeO}_6$ ) and tetrahedral ( $\text{FeO}_4$ ) coordination peaks of Fe<sup>40,41</sup>. Brownmillerite  $\text{Ca}_2\text{Fe}_2\text{O}_5$  consists of alternative layers of  $\text{FeO}_6$  octahedra and  $\text{FeO}_4$  tetrahedra as shown in Fig. 2a. In CFO sample, Fe  $2p_{3/2}$  and Fe  $2p_{1/2}$  peaks are appearing at 710.6 eV and 723.7 eV respectively with a binding energy difference  $\sim 13.1$  eV. A characteristic satellite peak corresponding to Fe is also observed at a difference of about 7.1 eV from Fe 2p peaks. For CCN50 sample Fe  $2p_{3/2}$  and Fe  $2p_{1/2}$  peaks appeared at 710.7 eV and 723.9 eV respectively with a B.E difference  $\sim 13.2$  eV. This indicates that in both samples Fe existed in 3+ oxidation state<sup>41,42</sup>. The presence of octahedra and tetrahedra coordination species of Fe in Fe 2p XPS spectra is a clear indication of oxygen vacancies in brownmillerite CFO and CCN50 samples<sup>35,43</sup>. The XPS spectra corresponding to O1s for both CFO and CCN50 samples were deconvoluted into two peaks [Fig. 3(c&f)] and named as OI and OII. The OI peak corresponding to lattice oxygen appears at 529.2 and 529.5 eV for CFO and CCN50 samples respectively. OII peaks appear at 531.5 and 531.8 eV respectively for both samples and is attributed to chemisorbed oxygen species<sup>42</sup>. The XPS spectra corresponding to C 1s and N 1s for CCN50 sample is shown in Fig. 3(g&h). For C 1s, XPS spectra was deconvoluted into three peaks located at 284.8 eV, 288.1 eV and 292.9 eV. The peak at 284.8 eV corresponds to surface adventitious carbon. The peaks

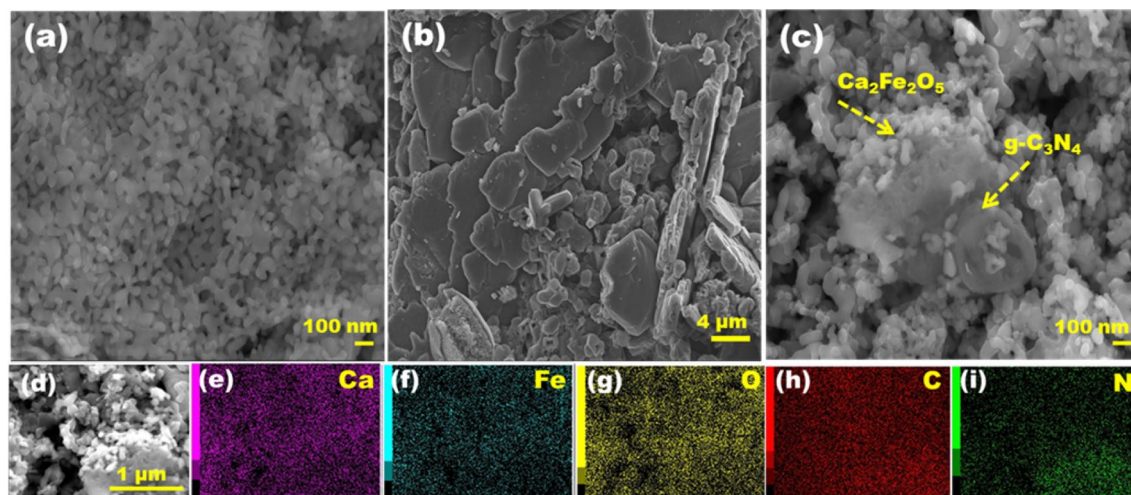


**Figure 2.** SEM images corresponding to (a-c) CFO,  $g\text{-C}_3\text{N}_4$  and CCN50 (d-i) EDS mapping images of CCN50 sample showing uniform distribution of Ca, Fe, O, C and N elements.

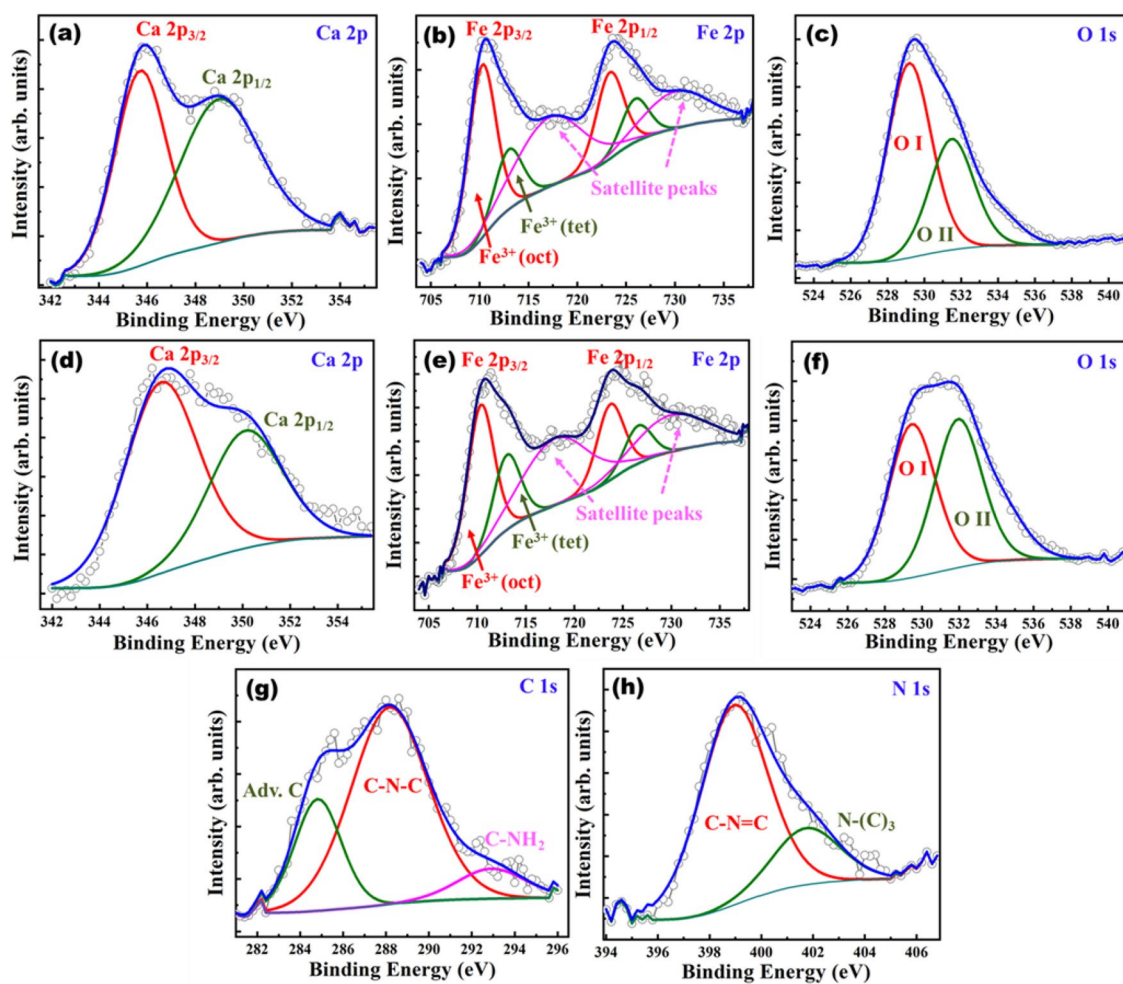


**Figure 3.** X-ray photoelectron spectra (de-convoluted) and the corresponding fits corresponding to CFO and CCN50 samples: in CFO (a) Ca 2p, (b) Fe 2p (c) O 1s and, in CCN50 (d) Ca 2p, (e) Fe 2p, (f) O 1s, (g) C 1s, (h) N 1s.

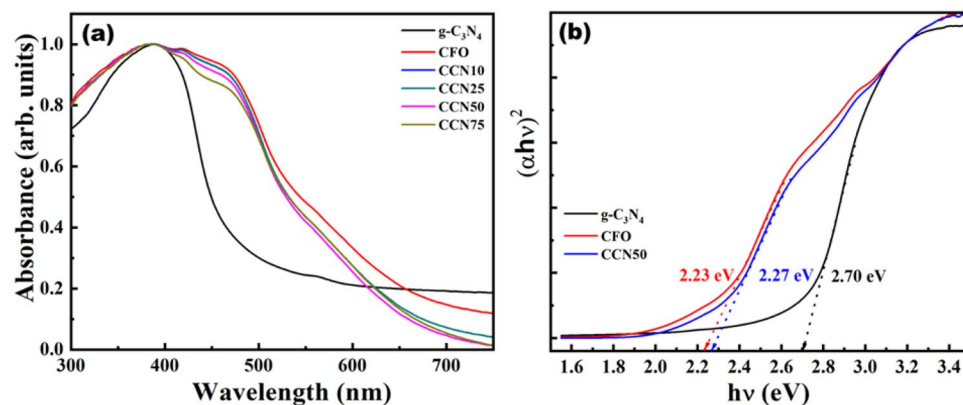


**Figure 4.** (a) UV–vis absorption spectroscopy of CFO,  $g\text{-C}_3\text{N}_4$ , CCN10, CCN25, CCN50 and CCN75 samples (b) Tauc plots corresponding to CFO,  $g\text{-C}_3\text{N}_4$  and CCN50.

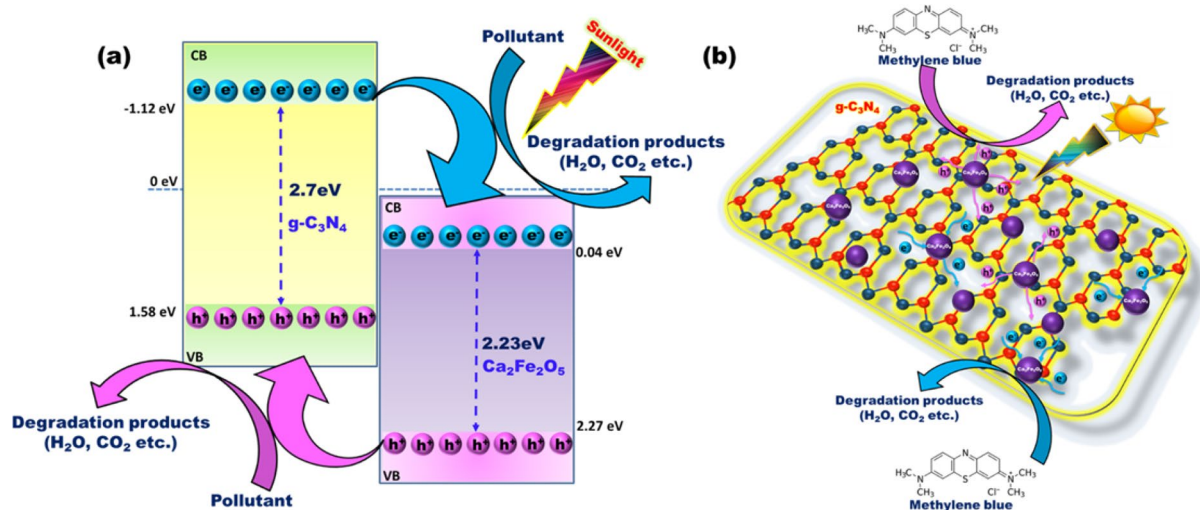


**Figure 5.** Schematic diagram of (a) Type-II heterostructure of  $g\text{-C}_3\text{N}_4/\text{CFO}$  (b) photocatalytic degradation mechanism of MB using  $g\text{-C}_3\text{N}_4/\text{CFO}$  heterostructure.

at 288.1 eV and 292.9 eV are attributed to  $sp^2$  hybridized (C–N–C) bond present in  $g\text{-C}_3\text{N}_4$  aromatic ring and the C–NH<sub>2</sub> bond respectively<sup>44–46</sup>. In case of N 1s, the XPS spectra could be deconvoluted into two peaks located at 398.9 eV and 401.7 eV. These two peaks can be attributed to  $sp^2$  hybridized (C–N=C) bond in the trizine rings and the N atoms in the ternary N–(C)<sub>3</sub><sup>46</sup>. These results confirm the presence of  $sp^2$ -bonded  $g\text{-C}_3\text{N}_4$  in CFO and formation of  $g\text{-C}_3\text{N}_4/\text{CFO}$  heterostructure.

The optical properties of  $g\text{-C}_3\text{N}_4/\text{CFO}$  heterostructures were studied using UV–visible absorbance spectroscopy. Optical absorbance of CFO,  $g\text{-C}_3\text{N}_4$  and  $g\text{-C}_3\text{N}_4/\text{CFO}$  heterostructures are shown in Fig. 4a. The absorbance of as synthesized heterostructures appears entirely in visible region and is highly desired for sunlight driven photocatalysis. The corresponding bandgap of CFO,  $g\text{-C}_3\text{N}_4$  and CCN50 obtained from Tauc plot is shown in Fig. 4b. The bandgap of  $g\text{-C}_3\text{N}_4$ , CFO and CCN50 are 2.7 eV, 2.23 eV and 2.27 eV respectively. Preliminary sunlight-driven catalytic activity of optimized  $g\text{-C}_3\text{N}_4/\text{CFO}$  heterostructures was investigated through photo-degradation of MB and BPA.

In order to enhance the photocatalytic activity over bare CFO and  $g\text{-C}_3\text{N}_4$ ,  $g\text{-C}_3\text{N}_4/\text{CFO}$  heterostructures were synthesized to reduce the recombination of photogenerated electron–hole pairs and effective charge separation.  $g\text{-C}_3\text{N}_4$  has a 2-dimensional graphite like structure constituting of  $\pi$ -conjugated systems, which are responsible for delocalization of electrons throughout the  $\pi$ -network<sup>47</sup>. The poor photocatalytic activity of  $g\text{-C}_3\text{N}_4$  is attributed to the recombination effects of photogenerated electron ( $e^-$ )–hole ( $h^+$ ) pairs due to coulombic forces<sup>48</sup>. Hence the optimum way to enhance the photocatalytic activity is through formation of composite or heterojunction of  $g\text{-C}_3\text{N}_4$  with other metal-oxides.

The photocatalytic degradation mechanism of CFO/ $g\text{-C}_3\text{N}_4$  heterostructures [Fig. 5(a&b)] is evaluated based on the energy band positions of valence band (VB) maxima and conduction band (CB) minima. The VB maximum and CB minimum positions of  $g\text{-C}_3\text{N}_4$  lie at  $\sim 1.58$  eV and  $\sim -1.12$  eV respectively, whereas for CFO they lie at 2.27 eV and 0.04 eV respectively, forming a type-II heterojunction between CFO and  $g\text{-C}_3\text{N}_4$  [Fig. 5a].

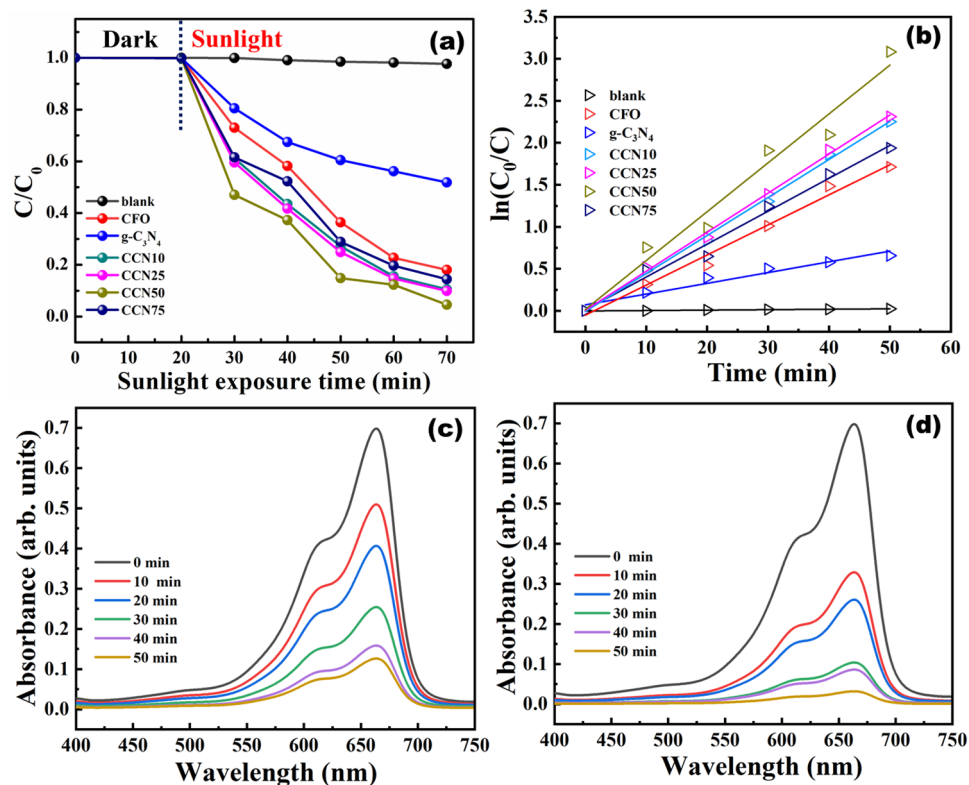


**Figure 6.** (a) Photocatalytic performance of activity of CFO,  $g-C_3N_4$ , CCN10, CCN25, CCN50 and CCN75 to degrade MB (b) corresponding reaction kinetics, and photodegradation profile of MB using (c) CFO (d) CCN50. (reaction conditions: pH = 7.2, temperature = 32 °C).

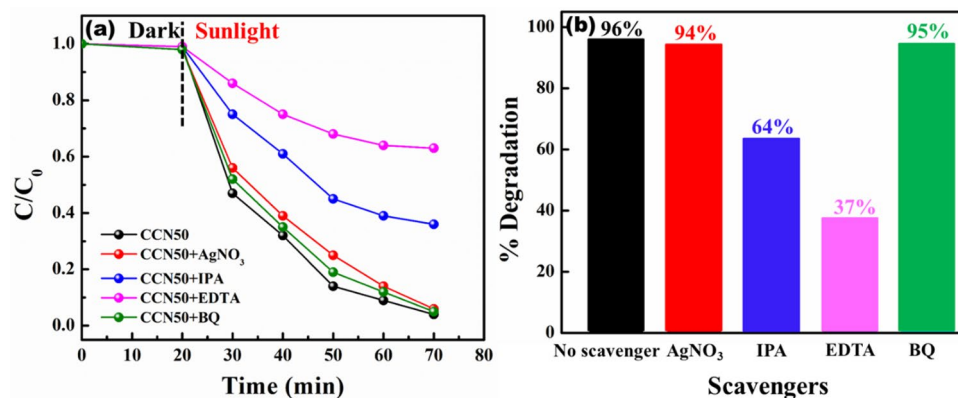


**Figure 7.** Comparisons of photocatalytic activities of CCN50 for the degradation of MB with and without various scavengers (a)  $C/C_0$  plots (b) percentage of degradation.

This type-II heterojunction helps to mitigate the  $e^-h^+$  pair recombination, thus improving the photocatalytic process. Individual optimization of photodegradation efficiency by CFO and  $g-C_3N_4$  samples provided a pathway to synthesize and investigate the  $g-C_3N_4$ /CFO composites. The  $g-C_3N_4$ /CFO composites are then used for degrading BPA under direct sunlight.

The percentage of degradation, first order rate constant plots and degradation profile of MB using CFO and CCN50 are shown in Fig. 6(a-d). Among the as synthesized samples, CCN50 showed higher photodegradation efficiency of about 96% with a rate constant  $0.058 \text{ min}^{-1}$ . This was found to be much higher than the photodegradation efficiencies of bare CFO and  $g-C_3N_4$  which showed photodegradation efficiencies of about 81.9% ( $0.035 \text{ min}^{-1}$ ) and 48.1% ( $0.013 \text{ min}^{-1}$ ) respectively. These studies imply that 50% of  $g-C_3N_4$  in CFO provides an optimal composition to form efficient heterostructure photocatalysts. An excessive  $g-C_3N_4$  content in  $g-C_3N_4$ /

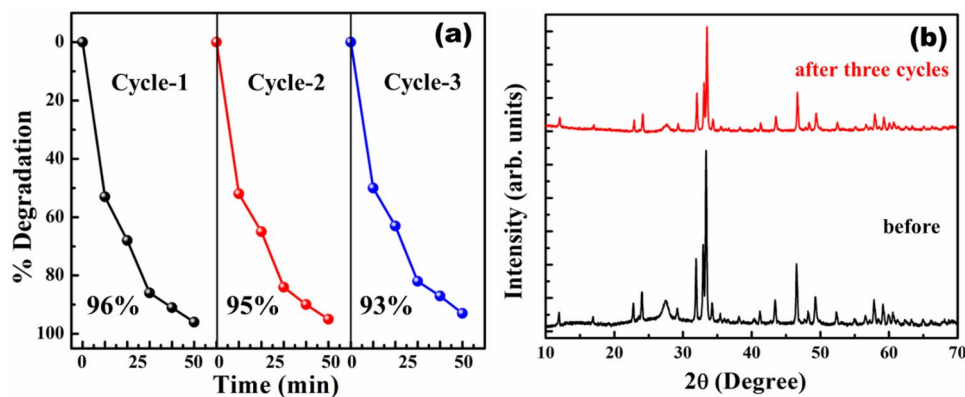


**Figure 8.** (a) The cyclic photocatalytic experiments for the degradation of MB using CCN50 (b) XRD patterns of CCN50 before, after the 3-cycles of photocatalytic degradation of MB.

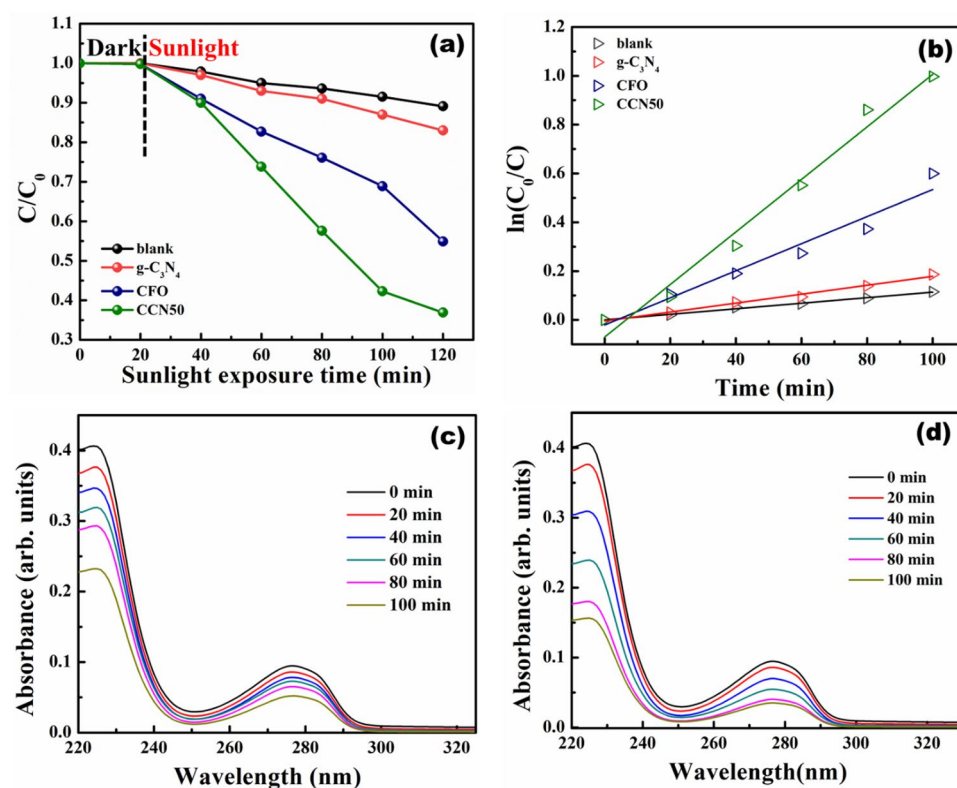


**Figure 9.** (a) Photocatalytic performance of CFO,  $g\text{-C}_3\text{N}_4$ , and CCN50 during degradation of BPA (b) corresponding reaction kinetics, and photodegradation profile of BPA using (a) CFO (b) CCN50.

CFO could cover the surface of CFO, which reduces the photon absorption of heterostructure and also the formation of heterojunction between  $g\text{-C}_3\text{N}_4$  and CFO could be suppressed by the inclusion of excessive  $g\text{-C}_3\text{N}_4$  due to aggregation phenomenon<sup>49</sup>. Less quantity of  $g\text{-C}_3\text{N}_4$  is a problem for efficient photodegradation, which may not suppress electron-hole recombination efficiently, hence the optimum content of  $g\text{-C}_3\text{N}_4$  loading plays a vital role in photodegradation performance of heterostructures. In this article 50% of  $g\text{-C}_3\text{N}_4$  content in CFO was found to be an optimal composition for efficient photodegradation.

The photocatalytic mechanism of  $g\text{-C}_3\text{N}_4/\text{Ca}_2\text{Fe}_2\text{O}_5$  (CCN50) heterostructure to degrade MB was explained in detail using active species trapping experiments (Fig. 7(a&b)). Various scavengers such as  $\text{AgNO}_3$  (1 mmol), isopropyl alcohol (IPA, 1 mmol), ethylenediaminetetraacetic acid (EDTA, 1 mmol), and benzoquinone (BQ, 1 mmol) are taken as electron ( $e^-$ ), hydroxyl radicals ( $\cdot\text{OH}$ ), holes ( $h^+$ ), and superoxide radicals ( $\text{O}_2^-$ ) trapping agents respectively. By adding electrons and superoxide radical trapping agents, the degradation of MB doesn't

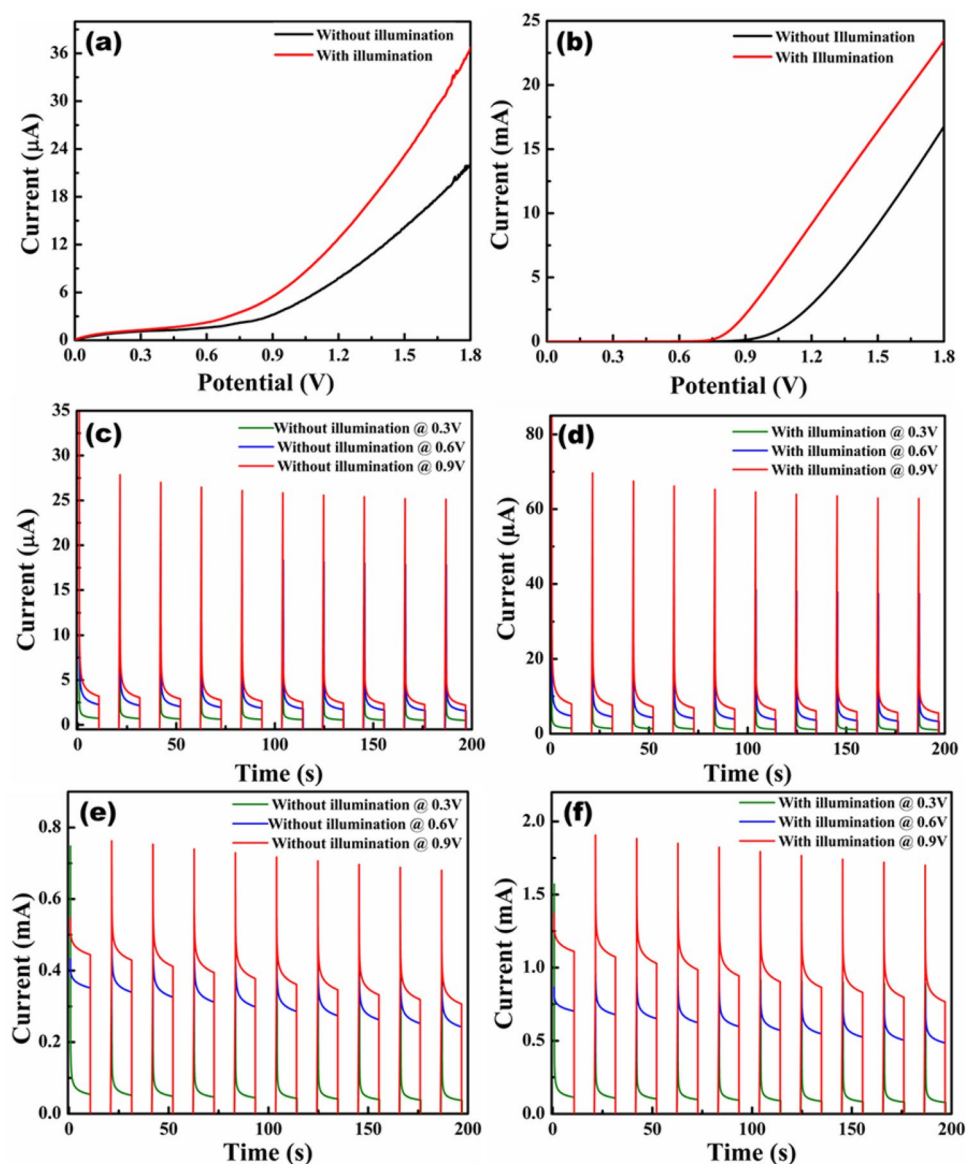


**Figure 10.** PEC characteristics of pure CFO and g-C<sub>3</sub>N<sub>4</sub>/CFO (CCN50) in 0.5 M KOH electrolyte under 100 mW/cm<sup>2</sup> light intensity (a and b) LSV curves of CFO and CCN50 with and without light. (c and d) CA plots of CFO with and without light. (e and f) CA plots of CCN50 with and without light.

change much but the photodegradation efficiency rapidly decreased to 64% and 37% from 96% by adding holes and hydroxyl radical trapping agents respectively. This implies that the photocatalytic mechanism is governed mainly by hydroxyl radicals ( $\bullet\text{OH}$ ) and holes ( $h^+$ ).

Recycling and stability studies were conducted on g-C<sub>3</sub>N<sub>4</sub>/Ca<sub>2</sub>Fe<sub>2</sub>O<sub>5</sub> (CCN50) heterostructure by degrading methylene blue (MB). The degradation efficiency of CCN50 was found to be reproducible up to three cycles (Fig. 8a). The slight reduction in efficiency in third cycle could be attributed to variation in sunlight intensity. No structural changes were observed in XRD pattern (Fig. 8b) of CCN50 post photodegradation. These studies revealed that as prepared heterostructures are stable and recyclable for practical usage.

The samples CFO, g-C<sub>3</sub>N<sub>4</sub> and optimized composite CCN50 were further utilized for degrading Bisphenol-A (BPA). BPA is widely used polycarbonate plasticizer to manufacture plastic containers to pack and carry food items<sup>50</sup> and was declared hazardous to human health, causing cancer, infertility, diabetes, and obesity etc.<sup>51,52</sup>

In the present work, BPA degradation was carried out under natural sunlight. The percentage of degradation, first order rate constant plots and degradation profile of BPA using CFO and CCN50 are shown in Fig. 9(a-d). BPA could be degraded up to 45.1%, 17% and 63.1% with a rate constant  $5.55 \times 10^{-3} \text{ min}^{-1}$ ,  $1.83 \times 10^{-3} \text{ min}^{-1}$  and  $10.76 \times 10^{-3} \text{ min}^{-1}$  using CFO, g-C<sub>3</sub>N<sub>4</sub> and CCN50 respectively. In the present study too, CCN50 showed better photodegradation performance as compared to CFO and g-C<sub>3</sub>N<sub>4</sub>. The photocatalytic performance of g-C<sub>3</sub>N<sub>4</sub>/CFO heterostructures were compared and tabulated in table S1.

Possible degradation pathway for BPA is shown in figure S1. CFO possesses holes ( $h^+$ ) and hydroxyl radicals as active species for photocatalytic degradation<sup>35</sup>. These active species attack the quaternary carbon in BPA

and form 2,2-bis(4-hydroxyphenyl)-1-propanol in Stage-I. The intermediate product further photocleaves into 4-hydroxybenzoate and 4-hydroxyacetophenone via C–C scission reaction in stage-II. These two intermediate products transform into aromatic formic and acetic acids in stage-III which further mineralizes into CO<sub>2</sub>, H<sub>2</sub>O and other degradation products in the final stage<sup>53</sup>. This process will continue until BPA degrades completely. The above studies reveal that g-C<sub>3</sub>N<sub>4</sub>/CFO composites are promising catalysts for degrading MB and BPA.

In order to examine the PEC properties of CFO and g-C<sub>3</sub>N<sub>4</sub>/CFO (CCN50) heterojunction, Linear sweep voltammetry (LSV) and Chronoamperometry (CA) studies were carried out with and without light illumination. From the LSV plots [Fig. 10(a & b)], it is clear that CCN50 electrode exhibits better photo response over pure CFO due to efficient charge separation and faster electron–hole transfer through Type-II heterojunction<sup>54</sup>. The photocurrents corresponding to pure CFO and CCN50 were observed from CA studies [Fig. 10(c–f)] at various potentials (0.3 V, 0.6 V and 0.9 V). The photocurrent for CCN50 was observed around 1.9 mA under constant illumination of light and for pure CFO electrode it was observed around 67.4 μA at 0.9 V. The photocurrent density improved remarkably in CCN50 heterojunction. The PEC studies revealed good photo response as well as efficient charge separation features of g-C<sub>3</sub>N<sub>4</sub>/CFO heterojunction over pure CFO. The photocatalytic and PEC studies reveal promising photoactivity of g-C<sub>3</sub>N<sub>4</sub>/CFO heterostructures as photoactive materials for solar energy harvesting applications.

## Conclusion

Brownmillerite CFO and g-C<sub>3</sub>N<sub>4</sub> heterostructures are developed using simple solid-state route. Structural, micro-structural and optical properties were analyzed using SEM, EDS, XPS and UV–Visible spectroscopy. Photocatalytic performance of as developed heterostructures were tested and compared by degrading organic effluents MB and BPA under sunlight. g-C<sub>3</sub>N<sub>4</sub>/CFO heterostructures show degradation efficiencies ~95.4% and ~63.1% for degrading MB and BPA respectively. The photoelectrochemical studies revealed higher photocurrents in g-C<sub>3</sub>N<sub>4</sub>/CFO heterostructures over CFO. The enhanced photodegradation efficiency was observed for g-C<sub>3</sub>N<sub>4</sub>/CFO heterostructures over bare Ca<sub>2</sub>Fe<sub>2</sub>O<sub>5</sub> and g-C<sub>3</sub>N<sub>4</sub>. The photoelectrochemical studies revealed higher photocurrents in g-C<sub>3</sub>N<sub>4</sub>/CFO heterostructures over CFO, which was attributed to suppression of electron–hole pair recombination. The systematic studies on these heterostructures revealed future potential of these newly developed heterostructures to be used for energy and environmental applications.

Received: 13 August 2021; Accepted: 17 September 2021

Published online: 04 October 2021

## References

- Hossain, M. F. in Sustainable Development for Mass Urbanization (ed Md Faruque Hossain) (Elsevier, 2019), 151–267.
- Abdellah, M. H., Nosier, S. A., El-Shazly, A. H. & Mubarak, A. A. Photocatalytic decolorization of methylene blue using TiO<sub>2</sub>/UV system enhanced by air sparging. *Alex. Eng. J.* **57**, 3727–3735 (2018).
- Gharbani, P., Tabatabaie, S. M. & Mehrizad, A. Removal of Congo red from textile wastewater by ozonation. *Int. J. Environ. Sci. Technol.* **5**, 495–500 (2008).
- Lin, Z. *et al.* A study on environmental bisphenol A pollution in plastics industry areas. *Water Air Soil Pollut.* **228**, 98 (2017).
- Almeida, S., Raposo, A., Almeida-González, M. & Carrascosa, C. Bisphenol A: Food exposure and impact on human health. *Compr. Rev. Food Sci. Food Saf.* **17**, 1503–1517 (2018).
- Mileva, G., Baker, S. L., Konkle, A. & Bielajew, C. Bisphenol-A: Epigenetic reprogramming and effects on reproduction and behavior. *Int. J. Environ. Res. Public Health* **11**, 7537–7561 (2014).
- Lellis, B., Fávoro-Polonio, C. Z., Pamphile, J. A. & Polonio, J. C. Effects of textile dyes on health and the environment and bioremediation potential of living organisms. *Biotechnol. Res. Innov.* **3**, 275–290 (2019).
- Abid, M. F., Zablouk, M. A. & Abid-Alameer, A. M. Experimental study of dye removal from industrial wastewater by membrane technologies of reverse osmosis and nanofiltration. *Iran. J. Environ. Health Sci. Eng.* **9**, 17 (2012).
- Bharathiraja, B., Jayamuthunagai, J., Praveenkumar, R. & Iyyappan, J. in Bioremediation: Applications for Environmental Protection and Management (eds Sunita J. Varjani, Avinash Kumar Agarwal, Edgard Gnansounou, & Baskar Gurunathan). (Springer Singapore, 2018), 243–252.
- Yagub, M. T., Sen, T. K., Afroze, S. & Ang, H. M. Dye and its removal from aqueous solution by adsorption: A review. *Adv. Coll. Interface. Sci.* **209**, 172–184 (2014).
- Konstantinou, I. K. & Albanis, T. A. TiO<sub>2</sub>-assisted photocatalytic degradation of azo dyes in aqueous solution: Kinetic and mechanistic investigations: A review. *Appl. Catal. B* **49**, 1–14 (2004).
- Sakthivel, S. *et al.* Solar photocatalytic degradation of azo dye: Comparison of photocatalytic efficiency of ZnO and TiO<sub>2</sub>. *Sol. Energy Mater. Sol. Cells* **77**, 65–82 (2003).
- Akpan, U. G. & Hameed, B. H. Parameters affecting the photocatalytic degradation of dyes using TiO<sub>2</sub>-based photocatalysts: A review. *J. Hazard. Mater.* **170**, 520–529 (2009).
- Tayeb, A. M., Tony, M. A. & Ismaeel, E. K. Engineered nanostructured ZnO for water remediation: Operational parameters effect, Box-Behnken design optimization and kinetic determinations. *Appl. Water Sci.* **9**, 43 (2019).
- Chakrabarti, S. & Dutta, B. K. Photocatalytic degradation of model textile dyes in wastewater using ZnO as semiconductor catalyst. *J. Hazard. Mater.* **112**, 269–278 (2004).
- Wang, X., Wang, F., Sang, Y. & Liu, H. Full-spectrum solar-light-activated photocatalysts for light-chemical energy conversion. *Adv. Energy Mater.* **7**, 1700473 (2017).
- Gu, D., Qin, Y., Wen, Y., Qin, L. & Seo, H. J. Photochemical and magnetic activities of FeTiO<sub>3</sub> nanoparticles by electro-spinning synthesis. *J. Taiwan Inst. Chem. Eng.* **78**, 431–437 (2017).
- Boudjellal, L., Belhadi, A., Brahimi, R., Boumaza, S. & Trari, M. Semiconducting and photoelectrochemical properties of the ilmenite CoTiO<sub>3</sub> prepared by wet method and its application for O<sub>2</sub> evolution under visible light. *J. Solid State Electrochem.* **24**, 357–364 (2020).
- Pugazhenthiran, N. *et al.* Sonochemical synthesis of porous NiTiO<sub>3</sub> nanorods for photocatalytic degradation of ceftiofur sodium. *Ultrason. Sonochem.* **35**, 342–350 (2017).
- Bhagwat, U. O., Wu, J. J., Asiri, A. M. & Anandan, S. Photocatalytic degradation of congo red using PbTiO<sub>3</sub> nanorods synthesized via a sonochemical approach. *ChemistrySelect* **3**, 11851–11858 (2018).

21. He, H. Y., Dong, W. X. & Zhang, G. H. Photodegradation of aqueous methyl orange on MnTiO<sub>3</sub> powder at different initial pH. *Res. Chem. Intermed.* **36**, 995–1001 (2010).
22. Aizat, A. *et al.* Photocatalytic degradation of phenol by LaFeO<sub>3</sub> nanocrystalline synthesized by gel combustion method via citric acid route. *SN Appl. Sci.* **1**, 91 (2018).
23. Ponraj, C., Vinitha, G. & Daniel, J. A review on the visible light active BiFeO<sub>3</sub> nanostructures as suitable photocatalyst in the degradation of different textile dyes. *Environ. Nanotechnol. Monit. Manag.* **7**, 110–112 (2017).
24. Sun, M. *et al.* Dye degradation activity and stability of perovskite-type LaCoO<sub>3-x</sub> (x=0~0.075). *Mater. Trans.* **51**, 2208–2214 (2010).
25. Ismael, M., Elhaddad, E., Taffa, D. H. & Wark, M. Solid state route for synthesis of YFeO<sub>3</sub>/g-C<sub>3</sub>N<sub>4</sub> composites and its visible light activity for degradation of organic pollutants. *Catal. Today* **313**, 47–54 (2018).
26. Wang, W., Li, G., Bai, Y., Yang, N. & Zhang, W. Surface photoelectric and photodegradation activities of AgNbO<sub>3</sub> synthesized by solvothermal method. *J. Phys. Chem. Solids* **72**, 1457–1461 (2011).
27. Torres-Martinez, L. M., Cruz-López, A., Juárez-Ramírez, I. & Meza-de la Rosa, M. E. Methylene blue degradation by NaTaO<sub>3</sub> sol-gel doped with Sm and La. *J. Hazard. Mater.* **165**, 774–779 (2009).
28. Li, Y., Yao, S., Wen, W., Xue, L. & Yan, Y. Sol-gel combustion synthesis and visible-light-driven photocatalytic property of perovskite LaNiO<sub>3</sub>. *J. Alloy. Compd.* **491**, 560–564 (2010).
29. Ola, O. & Maroto-Valer, M. M. Review of material design and reactor engineering on TiO<sub>2</sub> photocatalysis for CO<sub>2</sub> reduction. *J. Photochem. Photobiol., C* **24**, 16–42 (2015).
30. Jang, J. S., Kim, H. G. & Lee, J. S. Heterojunction semiconductors: A strategy to develop efficient photocatalytic materials for visible light water splitting. *Catal. Today* **185**, 270–277 (2012).
31. Liang, Q. *et al.* Recent advances of melamine self-assembled graphitic carbon nitride-based materials: Design, synthesis and application in energy and environment. *Chem. Eng. J.* **405**, 126951 (2021).
32. Fu, J., Yu, J., Jiang, C. & Cheng, B. g-C<sub>3</sub>N<sub>4</sub>-based heterostructured photocatalysts. *Adv. Energy Mater.* **8**, 1701503 (2018).
33. Patnaik, S., Martha, S. & Parida, K. M. An overview of the structural, textural and morphological modulations of g-C<sub>3</sub>N<sub>4</sub> towards photocatalytic hydrogen production. *RSC Adv.* **6**, 46929–46951 (2016).
34. Gupta, K., Singh, S. & Ramachandra Rao, M. S. Fast, reversible CO<sub>2</sub> capture in nanostructured Brownmillerite CaFeO<sub>2.5</sub>. *Nano Energy* **11**, 146–153 (2015).
35. Vavilapalli, D. S. *et al.* Nitrogen incorporated photoactive brownmillerite Ca<sub>2</sub>Fe<sub>2</sub>O<sub>5</sub> for energy and environmental applications. *Sci. Rep.* **10**, 2713 (2020).
36. Baijnath, T. P. & Basu, S. Cobalt and molybdenum co-doped Ca<sub>2</sub>Fe<sub>2</sub>O<sub>5</sub> cathode for solid oxide fuel cell. *Int. J. Hydrogen Energy* **44**, 10059–10070 (2019).
37. Tan, H. *et al.* Oxygen Vacancy Enhanced Photocatalytic Activity of Perovskite SrTiO<sub>3</sub>. *ACS Appl. Mater. Interfaces.* **6**, 19184–19190 (2014).
38. Jagannath, *et al.* HAXPES beamline PES-BL14 at the Indus-2 synchrotron radiation source. *J. Synchrotron Radiat.* **25**, 1541–1547 (2018).
39. Gu, Q. *et al.* Compact carbon nitride based copolymer films with controllable thickness for photoelectrochemical water splitting. *J. Mater. Chem. A* **5**, 19062–19071 (2017).
40. Wilson, D. & Langell, M. A. XPS analysis of oleylamine/oleic acid capped Fe<sub>3</sub>O<sub>4</sub> nanoparticles as a function of temperature. *Appl. Surf. Sci.* **303**, 6–13 (2014).
41. Vavilapalli, D. S. *et al.* Photoactive brownmillerite multiferroic KBiFe<sub>2</sub>O<sub>5</sub> and its potential application in sunlight-driven photocatalysis. *ACS Omega* **3**, 16643–16650 (2018).
42. Vavilapalli, D. S. *et al.* Multifunctional brownmillerite KBiFe<sub>2</sub>O<sub>5</sub>: Structural, magneto-dielectric, optical, photoelectrochemical studies and enhanced photocatalytic activity over perovskite BiFeO<sub>3</sub>. *Solar Energy Mater. Solar Cells* **200**, 109940 (2019).
43. Chen, M., Chen, D., Chang, M., Hu, H. & Xu, Q. New insight into hydrogen oxidation reaction on La<sub>0.5</sub>Sr<sub>0.7</sub>Fe<sub>0.7</sub>Cr<sub>0.3</sub>O<sub>3-δ</sub> perovskite as a solid oxide fuel cell anode. *J. Electrochem. Soc.* **164**, F405–F411 (2017).
44. Gao, D., Liu, Y., Liu, P., Si, M. & Xue, D. Atomically thin B doped g-C<sub>3</sub>N<sub>4</sub> nanosheets: High-temperature ferromagnetism and calculated half-metallicity. *Sci. Rep.* **6**, 35768 (2016).
45. Shen, L. *et al.* Black TiO<sub>2</sub> nanobelts/g-C<sub>3</sub>N<sub>4</sub> nanosheets laminated heterojunctions with efficient visible-light-driven photocatalytic performance. *Sci. Rep.* **7**, 41978 (2017).
46. Ma, F. *et al.* One-step exfoliation and fluorination of g-C<sub>3</sub>N<sub>4</sub> nanosheets with enhanced photocatalytic activities. *New J. Chem.* **41**, 3061–3067 (2017).
47. Babu, H. V., Bai, M. G. M. & Rajeswara Rao, M. Functional π-conjugated two-dimensional covalent organic frameworks. *ACS Appl. Mater. Interfaces* **11**, 11029–11060 (2019).
48. Fu, Y. *et al.* High-performance NiO/g-C<sub>3</sub>N<sub>4</sub> composites for visible-light-driven photocatalytic overall water splitting. *Inorg. Chem. Front.* **5**, 1646–1652 (2018).
49. Di, L., Yang, H., Xian, T. & Chen, X. Enhanced photocatalytic degradation activity of BiFeO<sub>3</sub> microspheres by decoration with g-C<sub>3</sub>N<sub>4</sub> nanoparticles. *Mater. Res.* **21**, 2018 (2018).
50. Hahladakis, J. N., Velis, C. A., Weber, R., Iacovidou, E. & Purnell, P. An overview of chemical additives present in plastics: Migration, release, fate and environmental impact during their use, disposal and recycling. *J. Hazard. Mater.* **344**, 179–199 (2018).
51. Ribeiro, E., Ladeira, C. & Viegas, S. Occupational exposure to bisphenol A (BPA): A reality that still needs to be unveiled. *Toxics* **5**, 22 (2017).
52. Diamanti-Kandarakis, E. *et al.* Endocrine-disrupting chemicals: An endocrine society scientific statement. *Endocr. Rev.* **30**, 293–342 (2009).
53. Zhao, C. *et al.* Activation of peroxymonosulfate by biochar-based catalysts and applications in the degradation of organic contaminants: A review. *Chem. Eng. J.* **416**, 128829 (2021).
54. Huang, Z. *et al.* Z-scheme NiTiO<sub>3</sub>/g-C<sub>3</sub>N<sub>4</sub> heterojunctions with enhanced photoelectrochemical and photocatalytic performances under visible LED light irradiation. *ACS Appl. Mater. Interfaces* **9**, 41120–41125 (2017).

## Acknowledgements

S. Singh would like to acknowledge DST/TMD-EWO/WTI/2K19/EWFH/2019/122, SERB (EMR/2017/000794) and DST Solar Energy Harnessing Center-DST/TMD/SERI/HUB/1(C). V. D. Sankar would like to acknowledge UGC for Senior Research Fellowship.

## Author contributions

V. D. Sankar. conceived and planned the present idea of work. Sankar developed the material and performed the experimental work as well as analyzed its structural, optical and catalytic studies. S.S. supervised the findings of this work and helped shape the manuscript. Shubra Singh encouraged to investigating the energy and environmental applications of as developed materials. XPS studies were performed by R.K.S., U.K.G. R.G. and

Muthuraaman performed the PEC studies and analyzed. Sankar, M.S.R. and S.S. contributed to the design and implementation of the research, analysis of the results and writing of the manuscript.

### Competing interests

The authors declare no competing interests.

### Additional information

**Supplementary Information** The online version contains supplementary material available at <https://doi.org/10.1038/s41598-021-99020-6>.

**Correspondence** and requests for materials should be addressed to S.S.

**Reprints and permissions information** is available at [www.nature.com/reprints](http://www.nature.com/reprints).

**Publisher's note** Springer Nature remains neutral with regard to jurisdictional claims in published maps and institutional affiliations.



**Open Access** This article is licensed under a Creative Commons Attribution 4.0 International License, which permits use, sharing, adaptation, distribution and reproduction in any medium or format, as long as you give appropriate credit to the original author(s) and the source, provide a link to the Creative Commons licence, and indicate if changes were made. The images or other third party material in this article are included in the article's Creative Commons licence, unless indicated otherwise in a credit line to the material. If material is not included in the article's Creative Commons licence and your intended use is not permitted by statutory regulation or exceeds the permitted use, you will need to obtain permission directly from the copyright holder. To view a copy of this licence, visit <http://creativecommons.org/licenses/by/4.0/>.

© The Author(s) 2021